Supporting Information

Ligand-mediated Formation of Cu/Metal Oxide Hybrid Nanocrystals with Tunable Number of Interfaces

Seyedeh Behnaz Varandili†, Dragos Stoian†, Jan Vavra†, James R. Pankhurst†, Raffaella Buonsanti†*

† Laboratory of Nanochemistry for Energy (LNCE), Institute of Chemical Sciences and Engineering, École Polytechnique Fédérale de Lausanne, CH-1950 Sion, Switzerland.

Additional Experimental Details

Chemicals

Cerium(III) nitrate hexahydrate ($Ce(NO_3)_3 \cdot 6H_2O$, 99%), Zinc(II) stearate ($Zn(St)_2$, technical grade), Zirconium(IV) isopropoxide isopropanol complex ($Zr(OCH(CH_3)_2)_4 \cdot (CH_3)_2CHOH$, 99.99%), Zirconium(IV) chloride ($ZrCl_4$, 99.9%), trioctylphosphine oxide ($\{CH_3(CH_2)_7\}_3PO$, or TOPO, 99%), oleic acid ($C_{17}H_{33}CO_2H$ or OLAC, 90%), 1-octadecene ($C_{18}H_{36}$ or ODE, 90%) and oleylamine ($C_{17}H_{33}NH_2$ or OLAM, 70%) were all purchased from Sigma-Aldrich and used as received.

Synthesis of the metal oxide seeds

Synthesis of CeO_2 NCs. Ceria seeds were synthesized by following a previously reported procedure[1]. 1 mmol of $Ce(NO_3)_3 \cdot 6H_2O$ was mixed with 1 mL of OLAM in 6.3 mL of ODE at room temperature and dissolved at 80°C for 30 min. Nanocrystals were grown by heating the mixture to 260°C for 2 h. The as-prepared nanocrystals were purified by washing, precipitation

and centrifugation, using ethanol, acetone and hexane in at least 4 cycles to remove any unreacted cerium precursor, surfactants, and excess ODE. The resultant dark brown precipitate was re-dispersed in hexane.

Synthesis of ZnO NCs. The zinc oxide seeds were synthesized following a previously reported procedure. 4 mmol of $Zn(St)_2$ and 30 ml OLAM were loaded into a 50 ml three neck flask and degassed under vacuum for 10 min without stirring at room temperature and with vigorous stirring at 110°C. The mixture then was heated to 240°C and maintained at that temperature for 20 min under N_2. Afterward, it was cooled slowly by removing the heating mantle. The reaction products were precipitated by addition of acetone and centrifuged three times for 5 min at 5000 rpm. The final NCs were then re-dispersed and stored in hexane.

Synthesis of ZrO_2 NCs. Zirconia seeds were synthesized according to colloidal methods previously reported by Hyeon et al.[2] 1 mmol of $ZrCl_4$ together with 0.8 mmol $Zr(OCH(CH_3)_2)_4 \cdot (CH_3)_2CHOH$ were added to 4 g of degassed TOPO at 60ºC in N_2 atmosphere. Then, the mixture was heated very slowly to 340ºC and kept for 2 hr before cooling to 60ºC. At this point, 2 mL of degassed acetone was injected and the resultant precipitate was recovered by centrifugation/washing cycles with acetone. Afterward, the NCs were re-dispersed in hexane. Finally, in order to assure the same ligand on the surface of all the seeds, we carried out a ligand exchange by using Meerwein salt ($[Me_3O][BF_4]$) as a stripping agent to replace the TOPO with OLAM.[3]

Characterization

X-ray photoelectron spectroscopy (XPS). XPS was carried out using VersaProbe II from Physical Electronics. Analysis was carried out using a monochromatic Al Kα X-ray source operating at 25 W with a beam size of 100 μm. The spherical mirror analyzer was set at 45º take-off angle with respect to the sample surface. The binding energy of the spectra were

calibrated by setting the C-C bound of the C 1s peak at 284.8 eV. In the fitting the FWHM of each component was limited to 3.5 eV and the fitting was mathematically optimized to maximize R-squared between the fit and the signal.

Fourier transform infra-red spectroscopy (FT-IR) was carried out on a Perkin Elmer Two spectrometer using an attenuated total reflectance (ATR) plate. Air and Toluene were used as background spectra for ligands and HNCs, respectively. Samples were prepared by drop-casting toluene suspensions of the HNCs directly onto the ATR plate and leaving to air-dry. Spectra were recorded with a resolution of 4 cm^{-1} and a total of 16 scans.

UV-vis absorption spectroscopy was done in transmission mode using a Perkin Elmer Lambda 950 spectrophotometer equipped with a tungsten halide lamp and a photomultiplier tube with a Peltier-cooled PbS detector. Samples were measured in screw-top, gas-tight quartz cuvettes (path = 10 mm). Background spectra were recorded for clean hexane solvent.

X-ray diffraction (XRD). X-ray diffraction was carried out on a Bruker D8 Advance diffractometer with a Cu K_α source equipped with a Lynxeye one-dimensional detector. The diffractometer operated at 40 kV and 40 mA with a Cu K_α source with wavelength of $\lambda = 1.54$ Å.

Electrocatalytic measurements

Details on the set-up. The geometric surface area for both working and counter electrodes was defined by an o-ring at 1 cm^2. A Selemion AMV anion-exchange membrane was used to separate the anodic and cathodic compartments. Each of the compartments was filled with electrolyte (0.1 M $KHCO_3$ solution, 2.1 mL in each half). The electrolyte solution was prepared by sparging a 0.05 M K_2CO_3 solution with CO_2 for 1 hour. During electrolysis, CO_2 was constantly bubbled through the electrolyte at a flow rate of 5 sccm to prevent depletion of CO_2 in the electrolyte and to enable continuous analysis of gaseous products using a gas

chromatograph. The flow rate of CO_2 was controlled with a mass flow-controller (Bronkhorst), and the gas was first humidified with water by passing it through a bubbler to minimize evaporation of the electrolyte.

Determination of the Electrochemical Active Surface Area. Double-layer capacitance measurements were carried out on HNCs in order to assess their surface areas. Using CO_2 saturated 0.1 M $KHCO_3$, cyclic voltammograms (CVs) were obtained at scan rates of 4, 8, 12, 16, 20, 24, 28 and 32 mV s^{-1}. A potential range from –0.15 to –0.2 V vs Ag/AgCl was chosen due to the absence of any Faradaic redox processes at these potentials. For each CV, the geometric current-densities at –0.18 V vs Ag/AgCl were recorded for both the cathodic ($J_{geom.,\ cath.}$) and anodic ($J_{geom.,\ anod.}$) sweeps; the difference between these two values gives a total value ($J_{geom.,\ T}$) for each scan rate (Eq. (S1)).

$$J_{geom.,T} = J_{geom.,anod.} - J_{geom.,cath.} \qquad \text{Eq. (S1)}$$

These current densities ($J_{geom.,\ T}$ / μA cm^{-2}) were plotted against the increasing scan rates (ν / V s^{-1}) to yield a linear plot whose slope gives the electrochemical double-layer capacitance ($C_{ECDL,\ sample}$ / μF cm^{-2}; R^2 typically greater than 0.99, Figure S9). By performing the same process for a clean glassy-carbon electrode, a reference capacitance value is obtained ($C_{ECDL,\ ref.}$ / μF cm^{-2}) from which a surface-roughness factor can be obtained (SRF, Eq. (S2)). By assuming the C_{ECDL} changes due to changes in the surface area (by addition of a nano-material to the substrate), the SRF can be multiplied by the geometric surface area ($A_{geom.}$ / cm^2) to give a more accurate value (A_{ECSA} / cm^2; Eq. (S3)).

$$SRF = \frac{C_{ECDL,sample}}{C_{ECDL,ref.}} \qquad \text{Eq. (S2)}$$

$$A_{ECSA} = SRF \times A_{geom} \qquad \text{Eq. (S3)}$$

***Operando* X-ray absorption spectroscopy (XAS)**

For standards and other *ex-situ* measurements (typically in pellet form and with the catalyst diluted in a light-matrix like e.g. boron nitride or cellulose to obtain an appropriate thickness, typically of 2-3 absorption lengths) we used a traditional system based on ionization chambers for transmission detection. CeO_2, $Ce(NO_3)_3$, Cu foil, Cu_2O, and CuO were used as standards for Ce and Cu edges, respectively. A Si(111) channel-cut monochromator was used to condition the beam from the corresponding bending magnet. The beam spot was focused using first a vertically collimating mirror and toroidal focusing mirror to approximately 300×200 μm^2 for the Cu K-edge (8.9789 keV), and slightly smaller size for Ce L3-edge (5.7234 keV) due to the miniaturized cell design. Fluorescence X-ray absorption near edge structure (XANES) spectra were acquired using the PIPS fluorescence detector to ensure an increased time-resolution (2 spectra per second). Data extraction, normalization, and averaging were performed using the beamline dedicated software for QEXAFS data analysis, ProXAS.[4,4] Finally, a multi-use beamline fixation support permits the cell alignment with respect to the incoming beam *via* the XYZ high-precision translation stage.

Multivariate curve resolution (MCR) analysis

We have made use of multivariate curve resolution using alternating least square mathematical algorithm (MCR-ALS) to analyze the huge amount of XANES spectra generated during the *operando* CO_2RR measurements. MCR-ALS is a data-reduction tool that can extract (even in a blind manner) kinetically pure component spectra and the corresponding concentration profiles out of an unresolved mixture.[5–7] The MCR-ALS model relies on the $\mathbf{D} = \mathbf{CS^T} + \mathbf{E}$ mathematical equation, with **D**: initial matrix composed of all collected spectra, **C**: extracted concentration profiles, **S**: extracted spectra profiles (**T** stands for transposed matrix), and **E**: error matrix containing the residuals and close to the experimental error. The MCR-ALS

graphical user interface (GUI) for MATLAB® used in this paper (freeware available at http://www.mcrals.info/) was applied on the Ce L3-edge time-resolved datasets from 5.690 to 5.770 keV by employing positive constraints for both spectra and concentration profiles, and closure constraints for the concentration profiles (i.e. constant concentration of the absorbing atoms throughout the experiment). Due to the nature of the system, we used the two standards for Ce^{4+} (CeO_2) and Ce^{3+} ($Ce(NO_3)_3$) as initial guess to model the kinetic evolution and speciation of the Ce atoms during the CO_2RR under an applied negative potential.

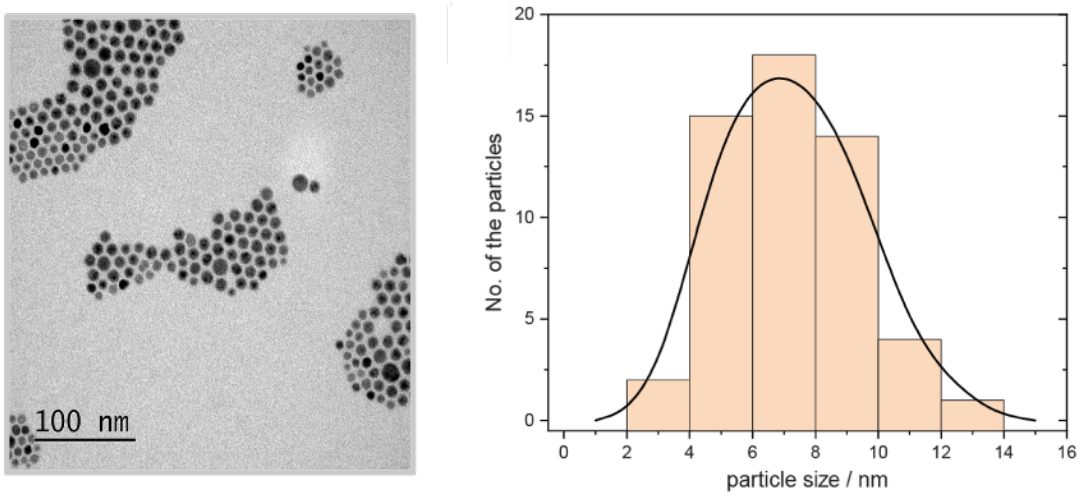

Figure S1. Representative TEM image and particle size distribution of the CeO_2 NCs used as seeds.

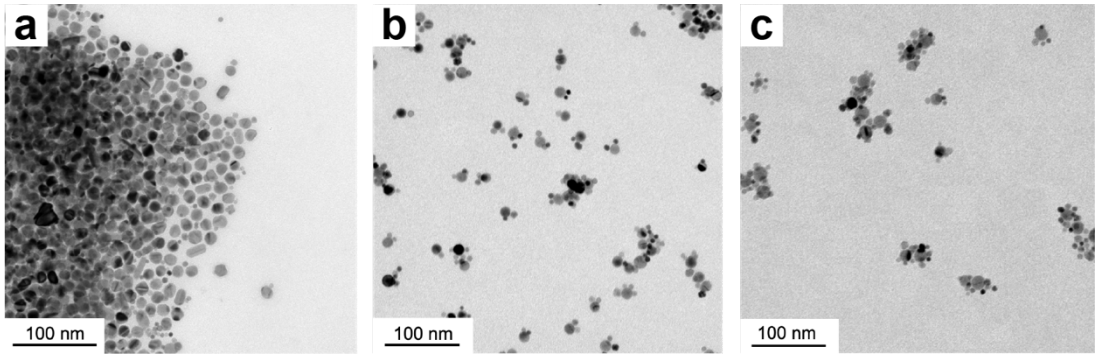

Figure S2. Representative TEM of (a) $Cu/(CeO_2)_1$, (b) $Cu/(CeO_2)_2$ and (c) $Cu/(CeO_2)_6$, synthesized in the presence of OLAC/OLAM, OLAC/OLAM /TOP and TOP only, respectively.

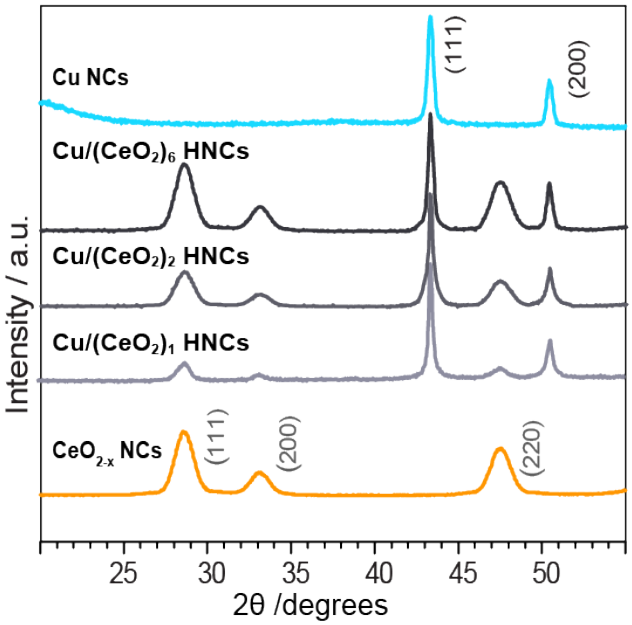

Figure S3. Representative XRD patterns of the Cu/CeO_2 HNCs reported along with the XRD patterns of Cu NCs and CeO_2 NCs of similar sizes to the HNC domains.

The data confirm the presence of Cu and CeO_2 domains in the HNCs without any peak shift possibly indicating doping or alloying. Additional structural data on $Cu/(CeO_2)_1$ are reported in our previous study.[8]

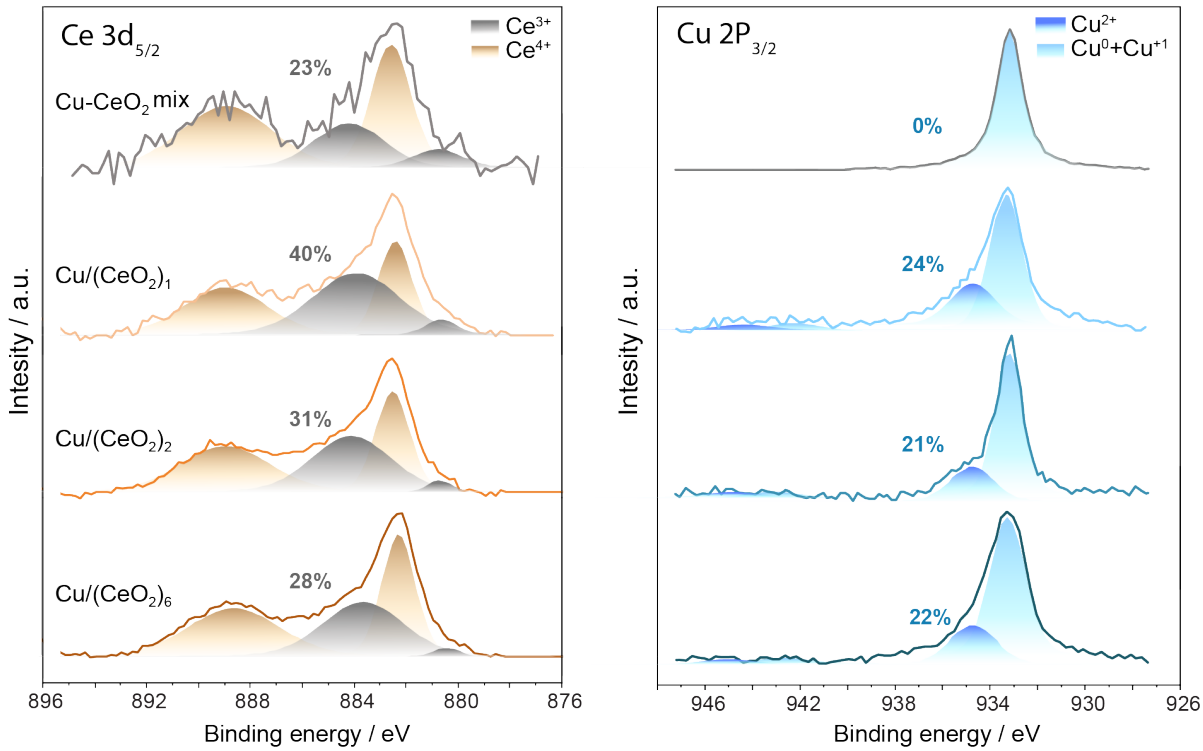

Figure S4. XPS plots of Ce $3d_{5/2}$ and Cu $2p_{3/2}$ spectra in Cu-CeO_2 mix, Cu/$(CeO_2)_1$, Cu/$(CeO_2)_2$ and Cu/$(CeO_2)_6$.

Compared to the physical mixture, an increase in the Ce^{3+}/Ce^{4+} ratio is observed in the HNCs. This result is consistent with the presence of an actual interface between Cu and CeO_2 facilitating the electron transfer between the two domains. As the number of junctions, and therefore the interfacial area, increases from Cu/$(CeO_2)_1$ to Cu/$(CeO_2)_2$ a decrease of such ratio is observed, then only a small difference is noticed between Cu/$(CeO_2)_2$ and Cu/$(CeO_2)_6$.

In their study on ceria-supported Pt nanoparticles, Lykhach et al. demonstrated that there is an intrinsic limit for charge transfer across metal/oxide interfaces.[9] They show that an optimal Pt particle density on the surface of the ceria support exist which maximizes the charge transfer. Above this, the partial charge per each Pt atom decreases and the overall number of transferred electrons approaches a limit.

While the value of such intrinsic limit is not known for the Cu/ceria interface, we can speculate that Cu/$(CeO_2)_1$ possesses the optimal interfacial area to maximize charge transfer, which then starts to decrease and to approach the intrinsic limit in Cu/$(CeO_2)_2$ and Cu/$(CeO_2)_6$.

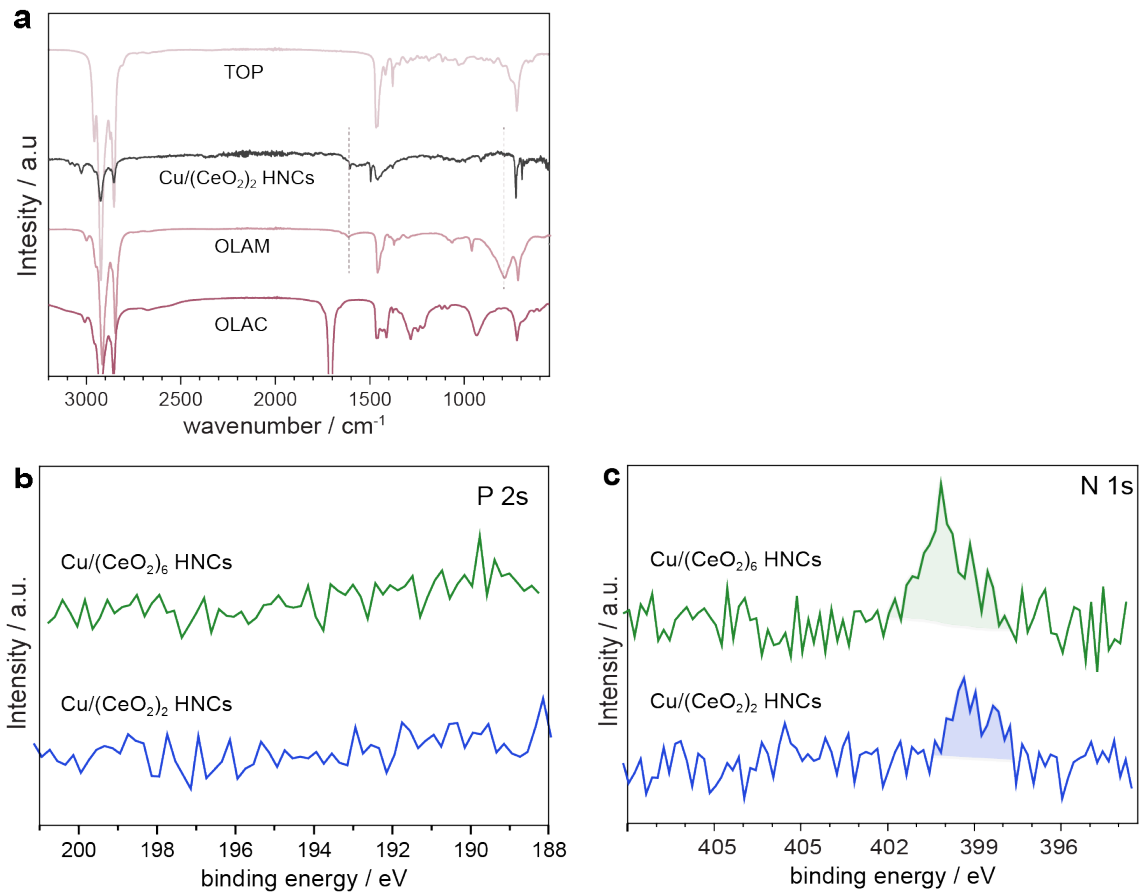

Figure S5. a) FT-IR spectra of $Cu/(CeO_2)_2$ HNCs along with OLAM, OLAC and TOP as references. b) XPS spectra of the P 2s and N 1s regions in $Cu/(CeO_2)_2$ and $Cu/(CeO_2)_6$ HNCs.

Keeping in mind that both the frequency and appearance of the ligand FTIR peaks are expected to change when binding on the NC surface, the spectrum of the HNCs in Figure S6a resembles more closely the one of the OLAM ligand. The presence of OLAM on the surface is also confirmed by XPS as only nitrogen was detected while no signal for phosphorous could be found. Note that in $Ce/(CeO_2)_6$ while no OLAM is nominally added, the CeO_2 seeds are functionalized with OLAM.

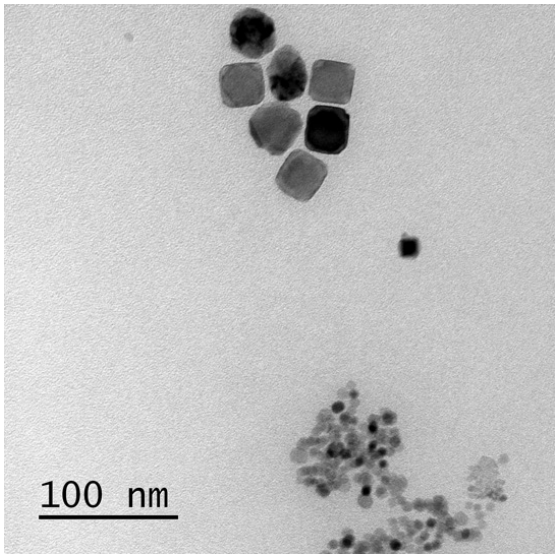

Figure S6. Representative TEM image of the Cu/CeO_2 sample obtained by performing the synthesis with TOP-coated CeO_2 NCs as seeds, instead of the OLAM-coated ones of the original procedure,while keeping all the other conditions the same.

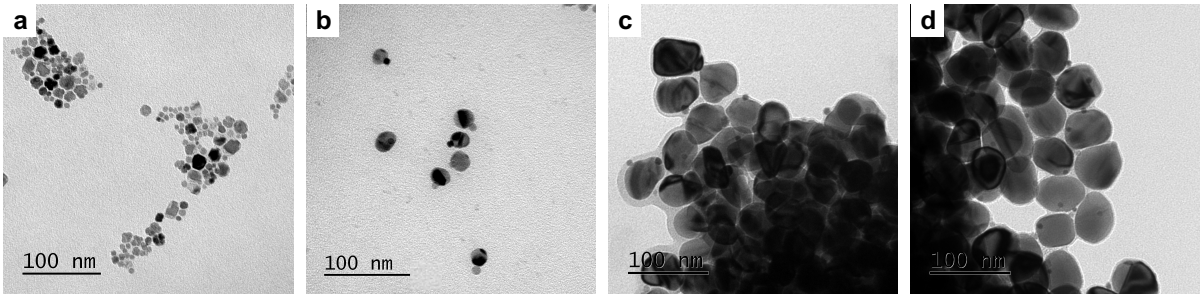

Figure S7. Representative TEM images of Cu/$(CeO_2)_1$ HNCs collected after a reaction time of (a) 75 s, (b) 150 a, (c) 300 s and (d) 600 s.

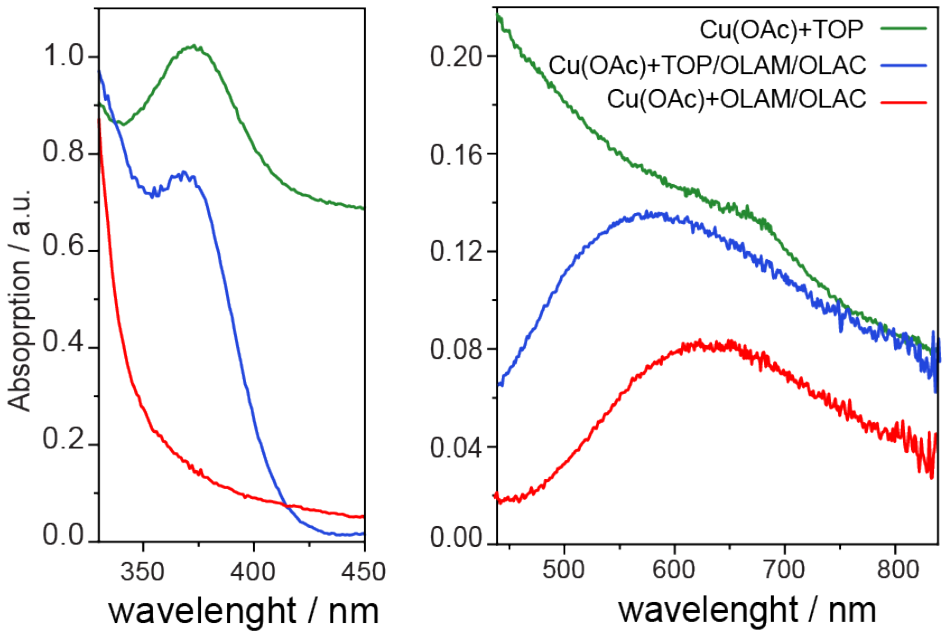

Figure S8. UV–vis absorption spectra collected upon mixing CuOAc with the various ligands, as denoted in the legend, in hexane at room temperature.

The UV-vis absorption spectrum for the $Cu(OAc)(TOP)_3$ shows a strong absorption band at 370 nm, which is assigned to ligand-to-metal charge transfer (LMCT). There are no significant spectral features in the 500-800 nm region, consistent with a stable +1 oxidation state. In comparison, solutions containing OLAM and OLAC that were left to turn blue displayed prominent absorption around 600 nm, consistent with the *d-d* transitions expected for Cu(II). Importantly, we highlight that this oxidation process occurs over a couple of days at room temperature, and not within the seconds timescale that is used in the NC synthesis.

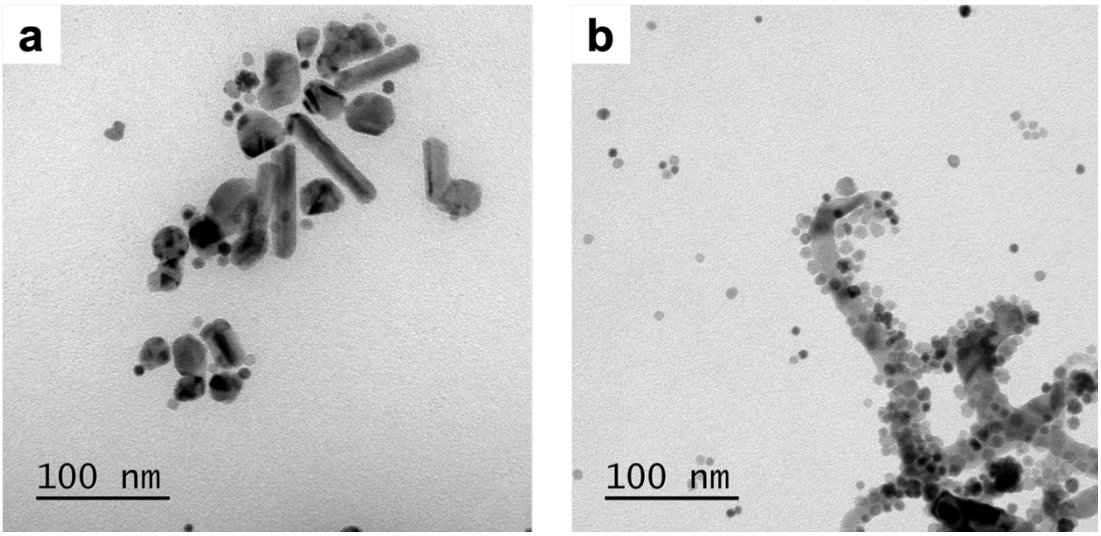

Figure S9. Representative TEM images of a Cu/CeO_2 sample formed by injecting the precursor solution containing CuOAc with (a) OLAM/OLAC and (b) TOP at 270ºC.

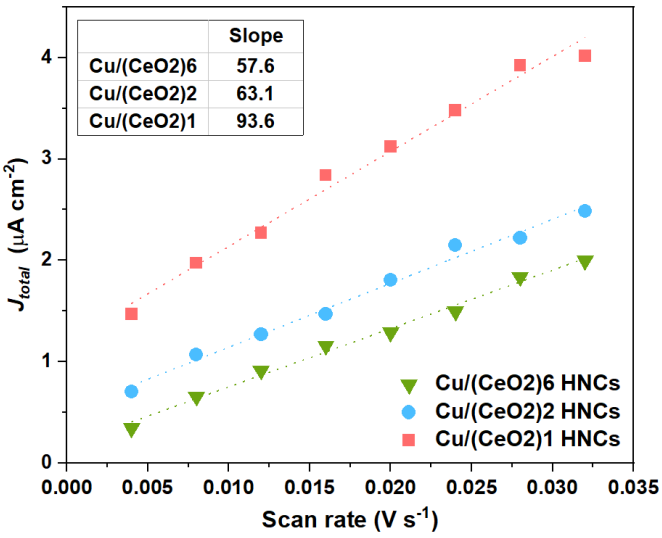

Figure S10. Current dependence on scan rate. The slopes indicate the electrochemical double-layer capacitance for each sample. Notes: Each point of the plots was calculated by subtraction of anodic and cathodic currents at -0.18 $V_{Ag/AgCl}$ for each scan rate.

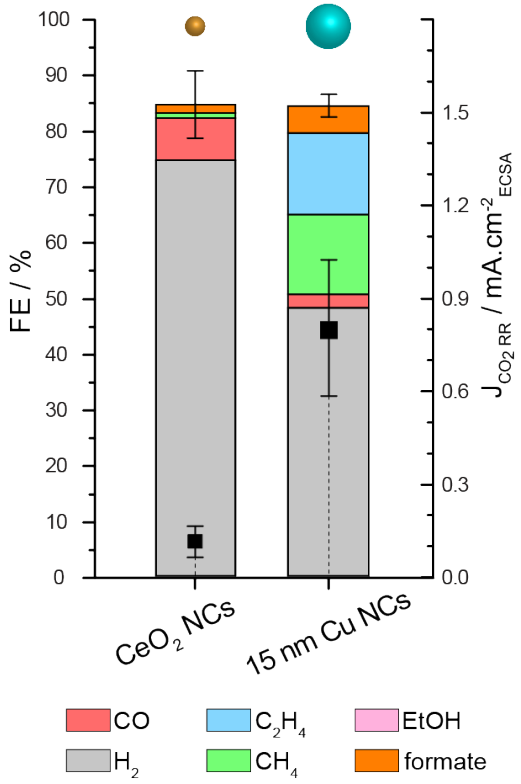

Figure S11. Faradic efficiencies and CO_2RR partial current-densities for 7 nm CeO_2 and 15 nm Cu deposited on a glassy-carbon substrate and measured at –1.2 V_{RHE} in 0.1 M $KHCO_3$.

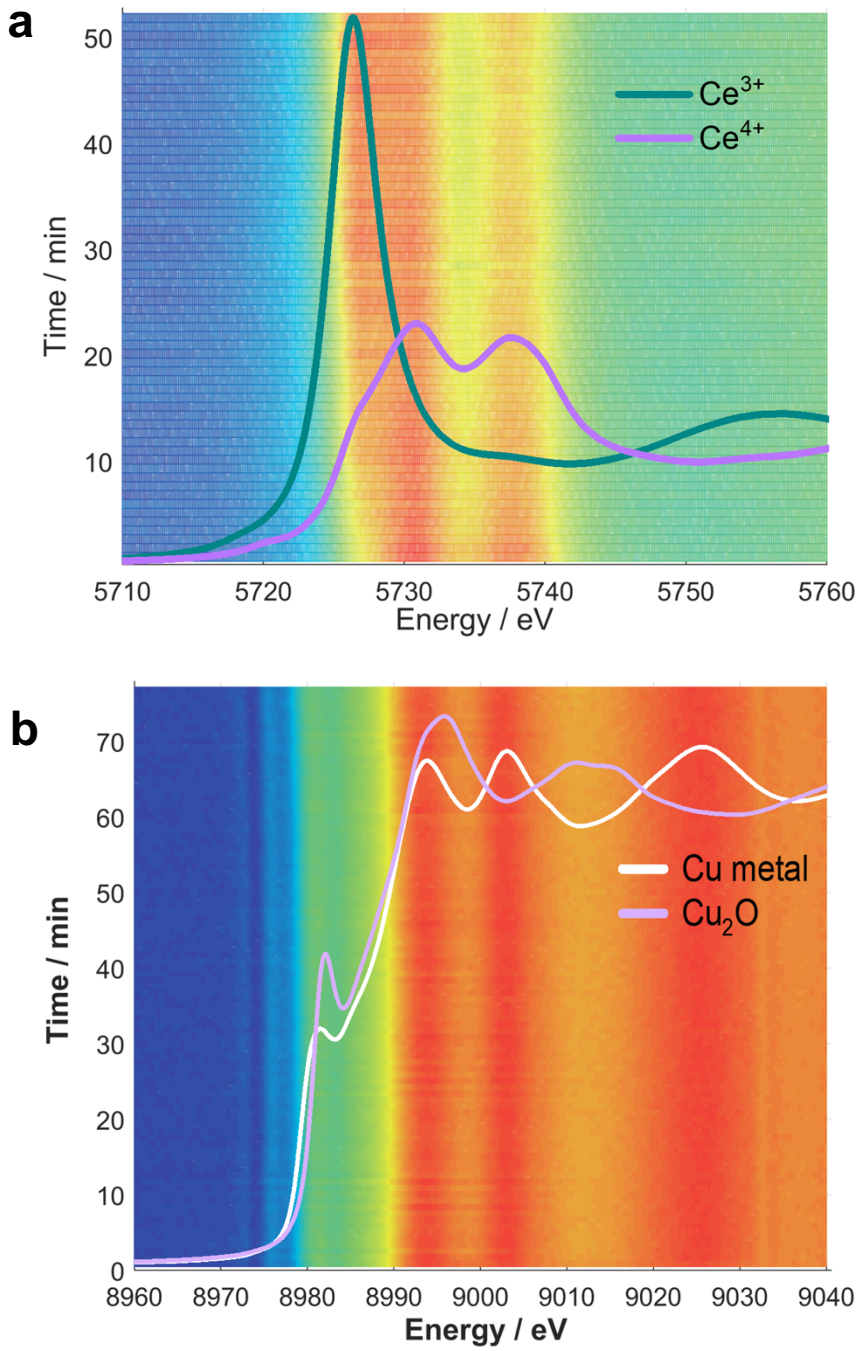

Figure S12. *Operando* CO_2RR experiment at -1.2 V_{RHE} for Cu/$(CeO_2)_1$ HNCs. a) Ce L_3-edge XANES of Cu/$(CeO_2)_1$ HNCs together with the references for $Ce(NO_3)_3$ and CeO_2. b) Cu K-edge XANES of Cu/$(CeO_2)_1$ HNCs together with the references for Cu_2O and metallic copper. Similar data were obtained for all samples.

References

1 S. S. Lee, W. Song, M. Cho, H. L. Puppala, P. Nguyen, H. Zhu, L. Segatori and V. L. Colvin, *ACS Nano*, 2013, **7**, 9693–9703.

2 J. Joo, T. Yu, Y. W. Kim, H. M. Park, F. Wu, J. Z. Zhang and T. Hyeon, *J. Am. Chem. Soc.*, 2003, **125**, 6553–6557.

3 E. L. Rosen, R. Buonsanti, A. Llordes, A. M. Sawvel, D. J. Milliron and B. A. Helms, *Angew. Chemie Int. Ed.*, 2012, **51**, 684–689.

4 A. H. Clark, J. Imbao, R. Frahm and M. Nachtegaal, *J. Synchrotron Radiat.*, 2020, **27**, 551–557.

5 C. Ruckebusch and L. Blanchet, *Anal. Chim. Acta*, 2013, **765**, 28–36.

6 A. De Juan, J. Jaumot and R. Tauler, *Anal. Methods*, 2014, **6**, 4964–4976.

7 J. Jaumot, R. Gargallo, A. De Juan and R. Tauler, *Chemom. Intell. Lab. Syst.*, 2005, **76**, 101–110.

8 S. B. Varandili, J. Huang, E. Oveisi, G. L. De Gregorio, M. Mensi, M. Strach, J. Vavra, C. Gadiyar, A. Bhowmik and R. Buonsanti, *ACS Catal.*, 2019, **9**, 5035–5046.

9 Y. Lykhach, S. M. Kozlov, T. Skála, A. Tovt, V. Stetsovych, N. Tsud, F. Dvořák, V. Johánek, A. Neitzel, J. Mysliveček, S. Fabris, V. Matolín, K. M. Neyman and J. Libuda, *Nat. Mater.*, 2016, **15**, 284–288.